Computed tomography simulation with superquadrics

Jiehua Zhu[a)]
Department of Mathematical Sciences, Georgia Southern University, Statesboro, Georgia 30460

Shiying Zhao[b)]
Department of Mathematics and Computer Science, University of Missouri - St. Louis, St. Louis, Missouri 63121

Yangbo Ye[c)] and Ge Wang[d)]
CT/Micro-CT Lab, Department of Radiology, The University of Iowa, Iowa City, Iowa 52242 and Department of Mathematics, The University of Iowa, Iowa City, Iowa 52242

(Received 25 May 2004; revised 21 June 2005; accepted for publication 23 July 2005; published 27 September 2005)

Accurate and efficient simulation of an x-ray transform for representative structures plays an important role in research and development of x-ray CT, for the evaluation and improvement of CT image reconstruction algorithms, in particular. Superquadrics are a family of three-dimensional objects, which can be used to model a variety of anatomical structures. In this paper, we propose an algorithm for the computation of x-ray transforms for superellipsoids and tori with a monochromatic x-ray. Their usefulness is demonstrated by projection and reconstruction of a superquadric-based thorax phantom. Our work indicates that superquadric modeling provides a more realistic visualization than quadratic modeling, and a faster computation than spline methods. © *2005 American Association of Physicists in Medicine*. [DOI: 10.1118/1.2040727]

Key words: computed tomography, x-ray transform, superquadrics, torus, cone beam

I. INTRODUCTION

In x-ray computed tomography (CT), measured data are typically in the form of the x-ray transform of an underlying distribution of x-ray linear attenuation coefficients, and can be well approximated, in the case of monochromatic x-ray, by line integrals of an object to be reconstructed. Modeling with various geometric shapes is necessary to represent anatomical structures and evaluate CT algorithms. Usually simple geometric shapes, such as spheres, disks, cylinders, and ellipsoids, are selected to quantify the performance of reconstruction algorithms in terms of image quality. But, like in computer vision applications, it is highly desirable that the shape modeling should be as realistic as possible while yet computationally manageable in the CT simulation. Because the human organs are irregular in their geometric shape, simplified models such as the traditional Shepp–Logan phantom[1] are often insufficient in accessing image quality in clinically oriented arenas.

For a model to be effective in CT simulation, we consider the following three factors: first, it is capable of representing a structure of interest in a somewhat realistic fashion; second, it allows an accurate and efficient computation of its x-ray transform; third, it facilitates or highlights the differences in the imaging performance of different CT algorithms. Overall, there are basically two categories of numerical phantoms in medical imaging research: voxel-based digital phantoms and primitive-based analytic phantoms. The voxel-based digital phantoms, such as anthropomorphic torso and head phantoms,[2] present objects by pixels in a given image resolution and thus prevent exact x-ray transforms. The primitive-based analytic phantoms describe the shapes or surfaces of objects using mathematical functions so that the x-ray transforms can be calculated more accurately. Currently, quadratic models and spline models are two popular methods in the development of primitive-based phantoms. The quadratic models[3] are traditionally used in CT simulations due to their efficiency in the computation of x-ray projections, but quadratic forms are too simple to describe the human organs well. The spline method,[4–6] on the other hand, is capable of producing more realistic phantoms, but usually involves much larger computation in generating x-ray projections.

Our main objective in this paper is to promote the use of superquadrics for CT simulation. Superquadrics are a family of 3D objects, which can be used to model a variety of objects. They have received significant attentions in the fields of computer vision, computer graphics, and robotics, because of their compact form and representation capabilities.[7] Although a superquadric-based heart model was developed for Monte Carlo simulation of radiological systems,[8,9] rather limited efforts have been made to utilize superquadrics directly for CT simulation. In this work we develop an algorithm of x-ray transform for superellipsoid and torus by applying the technique of ray tracing,[10] which is used mostly in geometric rendering. The application of superquadrics in CT simulation will give a more realistic visualization than quadratic models and a more efficient computation than spline-based methods.

In the next section, we outline the superellipsoid and torus models and propose the algorithms for the computation of the x-ray transforms for superellipsoids and tori. In the third section, we describe a thorax phantom consisting of superellipsoids and tori and present simulation results with the phantom to verify our algorithms. In the fourth section, we discuss relevant issues and conclude the paper. Finally, some properties of superellipsoids related to the computation of

the x-ray transform are presented in Appendix A, and parameters of representative components in the thorax phantom are listed in Appendix B.

II. X-RAY TRANSFORM FOR SUPERELLIPSOIDS AND TORI

A. Superellipsoid model

The superquadric model was introduced to the computer graphics field in 1981.[11,12] There are four types of superquadric models: superellipsoid, supertoroid, and superhyperboloid with one or two sheets. X-ray transforms of superellipsoid and torus modeling are discussed in this work.

A superellipsoid surface is defined by an implicit equation:

$$(|x/r_x|^{2/\varepsilon_2}+|y/r_y|^{2/\varepsilon_2})^{\varepsilon_2/\varepsilon_1}+|z/r_z|^{2/\varepsilon_1}=1, \tag{1}$$

where r_x, r_y, and r_z denote the scaling factors on x, y, and z axes; ε_1 and ε_2 the shape parameters of the superellipsoid cross section in the longitudinal and horizontal directions, respectively. More basics about superellipsoids can be referenced in Ref. 7. In our algorithm for x-ray transform for superellipsoids, the inside–outside function, defined by

$$F(\vec{p}) \equiv F(x,y,z)=(|x/r_x|^{2/\varepsilon_2}+|y/r_y|^{2/\varepsilon_2})^{\varepsilon_2/\varepsilon_1}+|z/r_z|^{2/\varepsilon_1}, \tag{2}$$

plays an important role. For each point $\vec{p}=(x,y,z)$, if $F(x,y,z)<1$, the point (x,y,z) is inside the superellipsoid; if $F(x,y,z)=1$, the point is on the surface of the superellipsoid; if $F(x,y,z)>1$, the point is outside the superellipsoid.

The convexity of the composite of the inside–outside function of a superellipsoid and parametric function of a line and the geometric bounds of superellipsoids are established in the next section for the computation of an x-ray transform.

B. X-ray transform for superellipsoids

Mathematically, the cone-beam x-ray transform is a collection of line integrals measured along a complex of x-ray paths with a common converging point where an x-ray source is located. For a phantom consisting of multiple objects of different shapes, we can determine the x-ray transform of each object, and sum all the individual transforms to obtain the composite transform because of the linearity of the x-ray transform.

The x-ray transform for a superellipsoid with a uniform density can be regarded as the product of the density and the length of the line segment inside the superellipsoid. Given an arbitrarily positioned superellipsoid and a ray in the three-dimensional space, an affine transformation can be applied in its local coordinate system so that the superellipsoid is centered at the origin with the same shape parameters but unit half-axes:

$$(x^{2/\varepsilon_2}+y^{2/\varepsilon_2})^{\varepsilon_2/\varepsilon_1}+z^{2/\varepsilon_1}=1, \tag{3}$$

where we have used the convention that $x^{2/\varepsilon_2}=(x^2)^{1/\varepsilon_2}$. Then the corresponding affine transformation applied to the ray results in a straight line given by

$$L_{\vec{a},\vec{b}}(t)=[a_1t+b_1,a_2t+b_2,a_3t+b_3], \tag{4}$$

where $\vec{a}=[a_1,a_2,a_3]$ and $\vec{b}=[b_1,b_2,b_3]$ are vectors in R^3. Ideally, if we can solve the following equation with respect to t:

$$[(a_1t+b_1)^{2/\varepsilon_2}+(a_2t+b_2)^{2/\varepsilon_2}]^{\varepsilon_2/\varepsilon_1}+(a_3t+b_3)^{2/\varepsilon_1}=1, \tag{5}$$

then the length of the line segment inside the superellipsoid can be computed from two neighboring roots.

Indeed, we can formulate the roots of (5) when ε_1 and ε_2 are taken as special values. For example, for the ellipsoid with $\varepsilon_1=\varepsilon_2=1$, the roots of (5) are

$$t=\frac{a_1b_1+a_2b_2+a_3b_3}{a_1^2+a_2^2+a_3^2} \pm \frac{\sqrt{(a_1b_1+a_2b_2+a_3b_3)^2-(a_1^2+a_2^2+a_3^2)(b_1^2+b_2^2+b_3^2-1)}}{a_1^2+a_2^2+a_3^2}. \tag{6}$$

When $[\varepsilon_1,\varepsilon_2]=[1,2]$, $[\varepsilon_1,\varepsilon_2]=[2,1]$ or $[\varepsilon_1,\varepsilon_2]=[2,2]$, the roots of (5) can also be explicitly obtained, but they are not included here for brevity. Nonetheless, for general values of the shape parameters, we have to find the roots of (5) numerically. In order to solve the nonlinear equation (5) numerically using the bisection method, we need to judge the existence of solutions, the number of solutions, and the appropriate initial interval. The properties of superellipsoids proved in Appendix A provide the theoretical base and guarantee for the following algorithm.

According to Theorem 1 in Sec. 1 of Appendix A, for $0<\varepsilon_1,\varepsilon_2<2$, the function

$$F[L_{\vec{a},\vec{b}}(t)]=[(a_1t+b_1)^{2/\varepsilon_2}+(a_2t+b_2)^{2/\varepsilon_2}]^{\varepsilon_2/\varepsilon_1}+(a_3t+b_3)^{2/\varepsilon_1}, \tag{7}$$

is convex with respect to t for all vectors $\vec{a}$ and $\vec{b}$, and must reach a unique minimum along each line $L_{\vec{a},\vec{b}}(t)$. Note that the function F is the inside–outside function of the superellipsoid. Therefore, the unique minimum can be used to determine whether the ray intersects the superellipsoid. If $\min(F[L_{\vec{a},\vec{b}}(t)])\geqslant 1$, the ray $L_{\vec{a},\vec{b}}(t)$ either misses or is tangential to the superellipsoid. If $\min(F[L_{\vec{a},\vec{b}}(t)])<1$, the ray intersects the superellipsoid. Furthermore, Theorem 3 in Sec. 1 of Appendix A indicates that the superellipsoid with $0<\varepsilon_1,\varepsilon_2<2$ is convex. Hence, there must be two distinct intersection points if the ray intersects with the superellipsoid, excluding tangential cases.

The geometric bounds of superellipsoids can refine the judgment about the existence of solutions and provide an initial bracketing interval for numerical solutions. According to Theorem 4 in Sec. 2 of Appendix A, for $1<\varepsilon_1,\varepsilon_2<2$, the superellipsoid is restricted within the ellipsoid. Therefore, if the ray $L_{\vec{a},\vec{b}}(t)$ does not intersect the ellipsoid, it would not intersect the superellipsoid (3). Similarly, for $0<\varepsilon_1,\varepsilon_2<2$, if the ray $L_{\vec{a},\vec{b}}(t)$ does not intersect the cube, it would not intersect the superellipsoid (3). We remark that the computa-

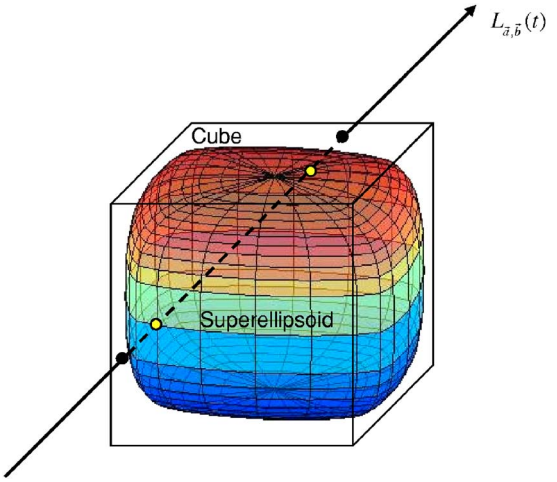

FIG. 1. Intersection of the ray $L_{\vec{a},\vec{b}}(t)$ with the cube and a superellipsoid.

tion of ellipsoid bounding boxes is about 25% faster than the cubic counterparts in our current implementation.

As shown in Fig. 1, we can first deduce the ray $L_{\vec{a},\vec{b}}(t)$ does not intersect the superellipsoid by finding that it does not intersect the ellipsoid if $1<\varepsilon_1,\varepsilon_2<2$ or the cube otherwise, and set the line integral along this ray to be zero. Otherwise, the ray probably intersects the superellipsoid. We then solve $(d/dt)F[L_{\vec{a},\vec{b}}(t)]=0$, find $\min(F[L_{\vec{a},\vec{b}}(t)])$ and determine whether the ray intersects the superellipsoid as above. If $\min(F[L_{\vec{a},\vec{b}}(t)])<1$, the ray intersects the superellipsoid at two distinct points, and we can solve $F[L_{\vec{a},\vec{b}}(t)]-1=0$ using the bisection method. The intersection points of the ray and the geometric bounds of the superellipsoid, as well as the solution to $(d/dt)F[L_{\vec{a},\vec{b}}(t)]=0$ can be used as the initial intervals for the bisection method. Figure 2 gives the block diagram. Note that although the numerical computation is involved in our algorithm, the result can be as accurate as we want up to the inherent precision of the computer.

In summary, the cubic or ellipsoid is first selected as bounding geometry for each superellipsoid modeling organ based on its shape parameters and tested to see whether it intersects the projection ray. In addition to the intersection of the ray and the bounding geometry, the minimum of the inside–outside function evaluated at the projection ray is used as the second criterion for the intersection of the ray and the superellipsoid. Only when this minimum is not greater than one, the intersection of the ray and the superellipsoid is guaranteed and then the bisection method is used to solve the intersection points.

C. Torus model and x-ray transform

A torus, as a special case of supertoroids, is a closed surface that fits the need to describe the objects with holes. In Cartesian coordinates, a torus centered at the origin is described by

$$\left[\sqrt{\left(\frac{x}{ar}\right)^2+\left(\frac{y}{br}\right)^2}-\frac{R}{r}\right]^2+\left(\frac{z}{cr}\right)^2=1, \tag{8}$$

where R is the radius from the center of the torus to the center of the torus tube, r is the radius of the torus tube, and a, b, and c are the scaling factors with x, y, and z axes.

The x-ray transform for a torus is the line segment of a ray through the torus. The number of intersection points of a ray with a torus varies from zero to four. So the x-ray transform for a torus is the sum of the distances between one or two pairs of neighboring intersection points.

For the standard torus of the form

$$\left[\sqrt{\left(\frac{x}{r}\right)^2+\left(\frac{y}{r}\right)^2}-\frac{R}{r}\right]^2+\left(\frac{z}{r}\right)^2=1, \tag{9}$$

and a ray described by (4), the intersections are determined by solving the following quadric equation using Francois Vieta's method:[13]

$$m_0t^4+m_1t^3+m_2t^2+m_3t+m_4=0, \tag{10}$$

where

$$\begin{aligned}
m_0&=(a_1^2+a_2^2+a_3^2)^2,\\
m_1&=4(a_1^2+a_2^2+a_3^2)(a_1b_1+a_2b_2+a_3b_3),\\
m_2&=2(a_1^2+a_2^2+a_3^2)(b_1^2+b_2^2+b_3^2-R^2-r^2)\\
&\quad+4[(a_1b_1+a_2b_2+a_3b_3)^2+a_3^2R^2],\\
m_3&=4[(a_1b_1+a_2b_2+a_3b_3)(b_1^2+b_2^2+b_3^2-R^2-r^2)\\
&\quad+2a_3b_3R^2],\\
m_4&=(b_1^2+b_2^2+b_3^2-R^2-r^2)^2+4(b_3-r^2)R^2.
\end{aligned} \tag{11}$$

Usually only a segment of a torus, instead of the whole torus, is needed in the phantom design. So the determination of suitable clip planes is important. For the segment we want, we compute the normal vectors of the clip planes for the two ends and then find the equations of two clip planes to compute the length of the segment.

III. NUMERICAL SIMULATION

To show the utility of superquadrics in CT simulation and verify the correctness of our x-ray transform algorithms for superellipsoids and tori, we designed a 3D thorax phantom using superellipsoids and tori. The reconstruction from the x-ray transform in the circular cone-beam geometry is based on the algorithm proposed by Feldkamp, Davis, and Kress.[14]

The thorax phantom includes the lungs, sternum, vertebra, and ribs. The 3D models for the thorax anatomy were originally provided by Image Processing Laboratory, University of Giessen.[15] Superellipsoids and tori were fit to the anatomical models. In total, 71 superellipsoids and tori were used, producing a superquadric model for the torso.[16] Clip planes were determined using the tangent plane where needed. Figure 3 displays the front view and side view of the 3D phantom. The two lungs are defined by two symmetric superel-

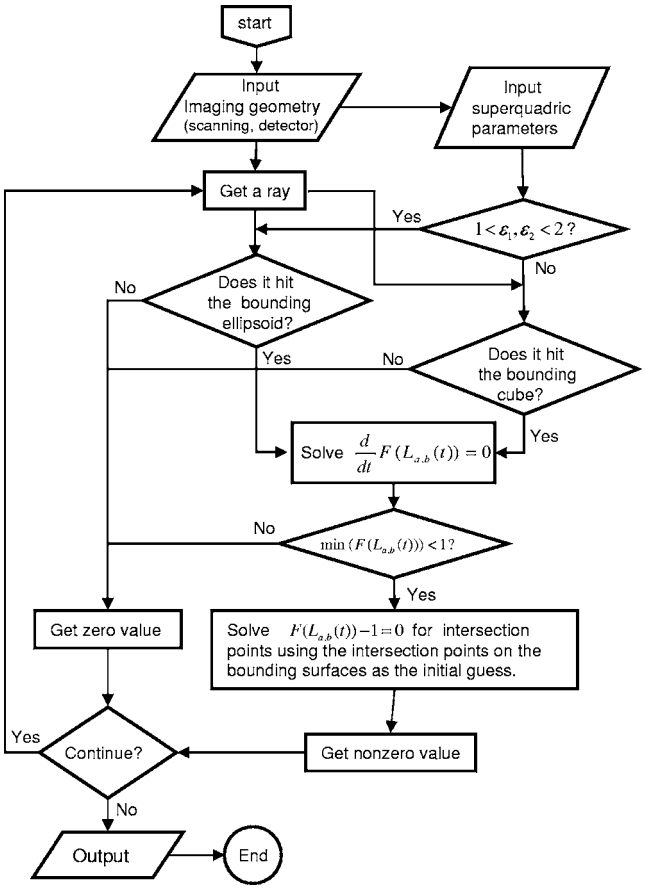

FIG. 2. Flow chart for computing the x-ray transform for a superellipsoid.

lipsoids, each blocked by an ellipsoid at the bottom, though this truncation is not shown in the 3D sketch. The sternum is described by three superellipsoids connected with a torus. The vertebrae are described by two embedded tori with the same center but different tubes with 14 segments being taken from the larger one. Each rib, on the right or the left, is described by one torus embedded with the torus of a smaller tube. The parameters of representative components are listed in Table I in Appendix B. Attenuation coefficients were determined in agreement with the FORBILD thorax phantom.[3] An appropriate precedence rule is applied for the intersection of the components to make sure the intended geometry is implemented.

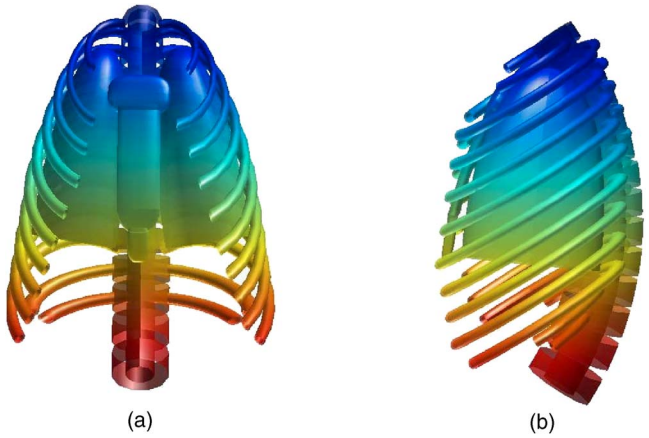

FIG. 3. 3D thorax phantom. (a) Front view; (b) side view.

The x-ray transform of the thorax phantom was calculated by superposition of the x-ray transform of each object using the algorithm described in the previous section. The diameter of the field of view was 250 mm, and the center of the phantom was at (150, 94, 250). The cone-beam projection data were generated in a matrix of size $256\times256\times256$, that is, the numbers of source positions per rotation as well as detectors along the horizontal direction and the vertical direction were all 256. After scaling to units at one unit per

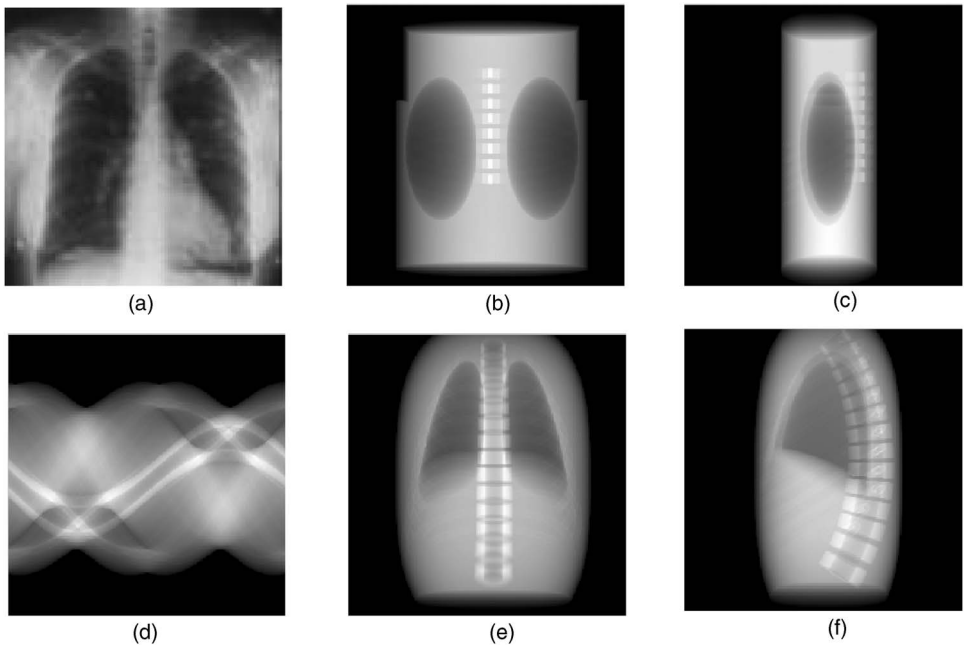

FIG. 4. Simulated projection images and actual CT lung image. (a) Posteroanterior projection of a normal chest. (b)–(c) Anterior and lateral projection of part of FORBILD thorax phantom. (d)–(f) Horizontal, anterior, and lateral projections of the superquadric-based thorax phantom.

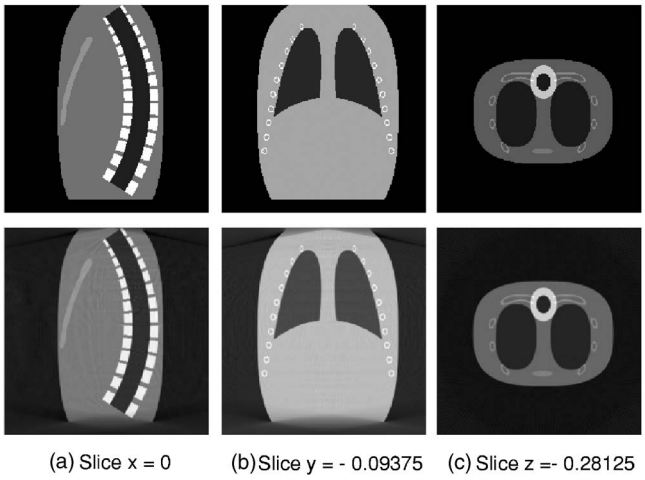

FIG. 5. Representative slices of the superquadrics-based thorax phantom. First row: original slices; Second row: reconstructed slices.

125 mm, the source-to-detector distance was 5 units while the radius of field-of-view is one unit for the circular cone-beam geometry. Reconstructed image volumes were generated in $256\times256\times256$ pixels. Figures 4(c)–4(e) show the projection images of the superquadric-based thorax phantom from different orientations. The FORBILD phantom and superquadric-based phantom are also compared with the actual CT scan in Fig. 4. In the FORBILD thorax phantom, the lungs, ribs, sternum, and vertebra are modeled by ellipsoids, boxes, and cylinders. It is noticeable that the superquadric phantom is much more improved in realism than the FORBILD phantom. The computational time for the cone-beam projection was compared between our superquadric-based thorax phantom and the FORBILD phantom with the same physical organs. Under the above geometry, it took approximately the same CPU time for computing the projection of size $256\times256\times256$.

Our in-house software package *TomoLab* was used to perform cone-beam image reconstruction from the simulated data. The representative slices $x=0$, $y=-0.093\,75$, and $z=-0.281\,25$ and the corresponding reconstructed images are shown in Fig. 5. The thorax phantom was successfully reconstructed from our simulated projection data, verifying the correctness of our algorithm.

IV. DISCUSSIONS AND CONCLUSION

Superquadrics can model a wide range of structures with only a small number of parameters. This characteristic makes superquadrics ideal to model human anatomy for CT simulation. Our superquadric-based thorax phantom has demonstrated the merits of our approach, which allows a more realistic impression and better simulation performance than is possible with quadratic modeling.

As a comparison, we briefly describe how line integrals are calculated in the spline method. The calculation of the projection data of the NCAT[5] phantom also uses a ray-tracing technique to find the intersection of a projection ray with the NURBS surfaces. A bounding box for each organ is first formed by selecting the maximum and minimum values from the matrix of control points defining the surface; then the bounding box is tested to see if it intersects the projection ray. If the projection ray does intersect the organ's bounding box, the projection ray probably intersects the surface of this organ. The Beizer Clipping algorithm[17] is used to iteratively calculate the intersection points. The NURBs surface is converted into Bezier form and then divided into subdivision recursively. The Bezier surfaces that do not intersect the ray are discarded. The surface that intersects the ray is tested for flatness. If it is not flat, the surface is subdivided into four subsurfaces and the tests for intersection and flatness continue.

The similarity between the calculation of projection data in superquadric modeling and spline modeling is the use of bounding geometry. Rather than an iterative procedure, we set bounds according to the shape parameters of superquadrics; also, we solve the equation using the bisection method after we confirm the existence of the intersection points. Therefore, in general, the superquadrics modeling provides much faster computations of the line integral than the spline method.

While in the initial tests we have used only superellipsoids and torus, in the future work we may extend our algorithm to allow for the complete family of superquadrics as well, especially supertoroids, which fits more complicated objects. Our next goal is to find the types and parameters of superquadrics from the real, volumetric CT/micro-CT data, compute the x-ray transform of more types of superquadrics precisely and efficiently, and further generalize our implementations from the current mathematics of line integrals to x-ray physics.

In this work, we have only considered the pure mathematical model of an x-ray transform. Therefore, all x-ray beams are simplified to line integrals. We will extend our work to involve a polychromatic x-ray beam in the future.

In conclusion, we have proposed an approach to use superquadrics for CT simulation, established several analytic properties of superellipsoids and tori, and developed an algorithm for a computation of the x-ray transform of a quite general type of superellipsoids and tori. Our algorithm has been theoretically justified and numerically verified in cone-beam reconstruction with a superquadric-based thorax phantom. The proposed algorithm has the potential to be a promising tool for CT simulation.

ACKNOWLEDGMENTS

This work was supported in part by NIH Grants No. R01 EB002667 and No. R21/R33 EB004287, by a Carver Scientific Research Initiative grant, and by a University of Iowa Mathematical and Physical Sciences Funding Program grant.

APPENDIX A: SOME PROPERTIES OF SUPERELLIPSOIDS

1. Convexity

Theorem 1: If $0<\varepsilon_1,\varepsilon_2<2$, the function $F[L_{\vec{a},\vec{b}}(t)]$ defined in (7) is convex with respect to t for all vectors $\vec{a}$ and $\vec{b}$.

Proof: Denote $F[L_{\vec{a},\vec{b}}(t)]$ in (7) by $f_{\varepsilon}(t)$ with $\vec{\varepsilon}=[\varepsilon_1,\varepsilon_2]$ and take the derivative with respect to t, by denoting $x=a_1t+b_1$, $y=a_2t+b_2$, and $z=a_3t+b_3$; we have

$$\frac{d}{dt}f_{\vec{\varepsilon}}(t)=\frac{2a_3}{\varepsilon_1}z^{2/\varepsilon_1-1}+\frac{2}{\varepsilon_1}(x^{2/\varepsilon_2}+y^{2/\varepsilon_2})^{\varepsilon_2/\varepsilon_1-1}\times(a_1x^{2/\varepsilon_2-1}+a_2y^{2/\varepsilon_2-1}),$$

and

$$\frac{d^2f_{\vec{\varepsilon}}(t)}{dt^2}=\frac{2a_3^2(2-\varepsilon_1)}{\varepsilon_1^2}z^{2(1/\varepsilon_1-1)}+\frac{2(2-\varepsilon_1)}{\varepsilon_1^2}(x^{2/\varepsilon_2}+y^{2/\varepsilon_2})^{\varepsilon_2/\varepsilon_1-1}(a_1x^{2/\varepsilon_2-1}+a_2y^{2/\varepsilon_2-1})^2+\frac{2(2-\varepsilon_2)}{\varepsilon_1\varepsilon_2}(x^{2/\varepsilon_2}+y^{2/\varepsilon_2})^{\varepsilon_2/\varepsilon_1-2}[a_1^2x^{2(1/\varepsilon_2-1)}y^{2/\varepsilon_2}+a_2^2x^{2/\varepsilon_2}y^{2(1/\varepsilon_2-1)}-2a_1a_2x^{2/\varepsilon_2-1}y^{2/\varepsilon_2-1}]\geqslant 0,$$

because every summand is non-negative, and the last one is due to

$$a_1^2x^{2(1/\varepsilon_2-1)}y^{2/\varepsilon_2}+a_2^2x^{2/\varepsilon_2}y^{2(1/\varepsilon_2-1)}-2a_1a_2x^{2/\varepsilon_2-1}y^{2/\varepsilon_2-1}=(a_1x^{1/\varepsilon_2-1}y^{1/\varepsilon_2}-a_2x^{1/\varepsilon_2}y^{1/\varepsilon_2-1})^2.$$

Therefore $f_{\vec{\varepsilon}}(t)$ is convex with respect to t.

Corollary 2: Along each line $L_{\vec{a},\vec{b}}(t)$, there must be a unique minimum of $F[L_{\vec{a},\vec{b}}(t)]$.

Theorem 3: For each given vector $\vec{a}$ and $\vec{b}$, the line $L_{\vec{a},\vec{b}}(t)$ intersects with the superellipsoid (3) if and only if $\min(F[L_{\vec{a},\vec{b}}(t)])\leqslant 1$.

Proof: If $\min(F[L_{\vec{a},\vec{b}}(t)])\leqslant 1$, then there is at least one point, say (x_0,y_0,z_0), on the line $L_{\vec{a},\vec{b}}(t)$ such that $F(x_0,y_0,z_0)\leqslant 1$. From the property of $F(x,y,z)$, this point is inside or on the superellipsoids. Hence, the line $L_{\vec{a},\vec{b}}(t)$ intersects with the superellipsoids. On the other hand, if the line intersects with the superellipsoid, there must be one or more points either inside or on the superellipsoid and $F(x,y,z)$ has values not greater than 1 at these points. That is, we must have $\min(F[L_{\vec{a},\vec{b}}(t)])\leqslant 1$.

2. Geometric bounds

Based on Eq. (3) of superellipsoids and the fact that $x^{2/\varepsilon_2}\geqslant 0$, $y^{2/\varepsilon_2}\geqslant 0$, and $z^{2/\varepsilon_2}\geqslant 0$, we have $(x^{2/\varepsilon_2}+y^{2/\varepsilon_2})^{\varepsilon_2/\varepsilon_1}\geqslant 0$, $z^{2/\varepsilon_1}\geqslant 0$, and $|x|\leqslant 1$, $|y|\leqslant 1$, $|z|\leqslant 1$. That is, the superellipsoids are completely contained by the unit cube. Moreover, in the case of $0<\varepsilon_1,\varepsilon_2<2$ we have the following refined geometric bounds.

Theorem 4: For $0<\varepsilon_1,\varepsilon_2<1$ the surface of superellipsoid (3) is bounded by the unit cube and an ellipsoid with $\varepsilon_1=\varepsilon_2=1$ in (3). For $1<\varepsilon_1,\varepsilon_2<2$, the surface of superellipsoid (3) is bounded by an ellipsoid with $\varepsilon_1=\varepsilon_2=1$ in (3) and a diamond with $\varepsilon_1=\varepsilon_2=2$ in (3).

Proof: Suppose $\vec{p}=(x,y,z)$ is a given point on the surface of ellipsoid

$$x^2+y^2+z^2=1. \tag{A1}$$

If such a point has one of the three components x, y, and z equal to one, then it can be easily proved that the other two components should be zero. That is, it must be on the surfaces of the cube, ellipsoid and diamond defined in this theorem.

From now on, we assume that $|x|<1$, $|y|<1$ and $|z|<1$. Let

$$f_{\vec{p}}(\varepsilon_1,\varepsilon_2)=(A^{1/\varepsilon_2}+B^{1/\varepsilon_2})^{\varepsilon_2/\varepsilon_1}+C^{1/\varepsilon_1}, \tag{A2}$$

where $A=x^2$, $B=y^2$, and $C=z^2$. Clearly, A, B, and C are non-negative and less than one.

Take partial derivatives with respect to ε_1 and ε_2,

$$\frac{\partial f_{\vec{p}}(\varepsilon_1,\varepsilon_2)}{\partial\varepsilon_1}=-\frac{1}{\varepsilon_1}((A^{1/\varepsilon_2}+B^{1/\varepsilon_2})^{\varepsilon_2/\varepsilon_1}\ln(A^{1/\varepsilon_2}+B^{1/\varepsilon_2})^{\varepsilon_2/\varepsilon_1}+C^{1/\varepsilon_1}\ln C^{1/\varepsilon_1}), \tag{A3}$$

$$\frac{\partial f_{\vec{p}}(\varepsilon_1,\varepsilon_2)}{\partial\varepsilon_2}=-\frac{(A^{1/\varepsilon_2}+B^{1/\varepsilon_2})^{\varepsilon_2/\varepsilon_1-1}}{\varepsilon_1}[A^{1/\varepsilon_2}\ln A^{1/\varepsilon_2}+B^{1/\varepsilon_2}\ln B^{1/\varepsilon_2}-(A^{1/\varepsilon_2}+B^{1/\varepsilon_2})\ln(A^{1/\varepsilon_2}+B^{1/\varepsilon_2})]. \tag{A4}$$

For any $0<\varepsilon_1,\varepsilon_2<2$, we deduce that $A^{1/\varepsilon_2}\ln A^{1/\varepsilon_2}+B^{1/\varepsilon_2}\ln B^{1/\varepsilon_2}\leqslant(A^{1/\varepsilon_2}+B^{1/\varepsilon_2})\ln(A^{1/\varepsilon_2}+B^{1/\varepsilon_2})$ and, furthermore, $\partial f_{\vec{p}}(\varepsilon_1,\varepsilon_2)/\partial\varepsilon_2\geqslant 0$.

If $0<\varepsilon_1,\varepsilon_2<1$, we have $A^{1/\varepsilon_2}+B^{1/\varepsilon_2}\leqslant A+B\leqslant 1$, and $\ln(A^{1/\varepsilon_2}+B^{1/\varepsilon_2})^{\varepsilon_2/\varepsilon_1}\leqslant 0$. An investigation of the sign of each term in (A3) gives $\partial f_{\vec{p}}(\varepsilon_1,\varepsilon_2)/\partial\varepsilon_1\geqslant 0$. Therefore, $f_{\vec{p}}(\varepsilon_1,\varepsilon_2)\leqslant f_{\vec{p}}(1,1)=1$. This implies that the point $\vec{p}=(x,y,z)$ is inside or on the surface of the superellipsoid with parameters ε_1 and ε_2. Therefore, the surface of the superellipsoid with $0<\varepsilon_1,\varepsilon_2<1$ is bounded by that of the ellipsoid with $\varepsilon_1=\varepsilon_2=1$ in (3) and the cube $|x|<1$, $|y|<1$ and $|z|<1$.

If $1<\varepsilon_1,\varepsilon_2<2$, we have

$$f_{\vec{p}}(\varepsilon_1,\varepsilon_2)=(A^{1/\varepsilon_2}+B^{1/\varepsilon_2})^{\varepsilon_2/\varepsilon_1}+C^{1/\varepsilon_1}\geqslant 1. \tag{A5}$$

Otherwise, $\partial f_{\vec{p}}(\varepsilon_1,\varepsilon_2)/\partial\varepsilon_1\geqslant 0$, which leads to a contradiction. So the point $\vec{p}=(x,y,z)$ on the ellipsoid (A1) is outside or on the superellipsoid, i.e., the superellipsoid with $1<\varepsilon_1,\varepsilon_2<2$ is contained by the ellipsoid (A1). On the other hand, for any point $\vec{q}=(\tilde{x},\tilde{y},\tilde{z})$ on the diamond with $\varepsilon_1=\varepsilon_2=2$ in (3), i.e., $|\tilde{x}|+|\tilde{y}|+|\tilde{z}|=1$; denoting

$$f_{\vec{q}}(\varepsilon_1,\varepsilon_2)=(\tilde{A}^{1/\varepsilon_2}+\tilde{B}^{1/\varepsilon_2})^{\varepsilon_2/\varepsilon_1}+\tilde{C}^{1/\varepsilon_1}, \tag{A6}$$

with $\tilde{A}=\tilde{x}^2$, $\tilde{B}=\tilde{y}^2$, and $\tilde{C}=\tilde{z}^2$; we have

$$\frac{\partial f_{\vec{q}}(\varepsilon_1,\varepsilon_2)}{\partial\varepsilon_1}=-\frac{1}{\varepsilon_1}[(\tilde{A}^{1/\varepsilon_2}+\tilde{B}^{1/\varepsilon_2})^{\varepsilon_2/\varepsilon_1}\ln(\tilde{A}^{1/\varepsilon_2}+\tilde{B}^{1/\varepsilon_2})^{\varepsilon_2/\varepsilon_1}+\tilde{C}^{1/\varepsilon_1}\ln\tilde{C}^{1/\varepsilon_1}]\geqslant 0.$$

Therefore, $f_{\vec{q}}(\varepsilon_1,\varepsilon_2)\leqslant f(2,2)=1$, which implies that the point $\vec{q}=(\tilde{x},\tilde{y},\tilde{z})$ lies inside or on the superellipsoids. Therefore, the surface of superellipsoid with $1<\varepsilon_1,\varepsilon_2<2$ is bounded by that of the ellipsoid with $\varepsilon_1=\varepsilon_2=1$ and the diamond with $\varepsilon_1=\varepsilon_2=2$ in (3).

APPENDIX B: SUPERQUADRIC-BASED THORAX PHANTOM

TABLE I. Parameters of representative components in the thorax phantom.

Object	Params[a]	Center	Half-axis	Rotation	Clip plane
			Lungs		
Super-ellipsoid	[1.15, 0.80]	[114, 88, 250]	[24.0, 39.0, 100.0]	[5.06, −8.97, −0.79]	$z<275$
Super-ellipsoid	[1.00, 1.00]	[115, 85, 295]	[55.0, 110.0, 64.0]	[0.00, −50.00, 0.00]	$x<150, z<280$
Super-ellipsoid	[1.15, 0.80]	[186, 88, 250]	[24.0, 39.0, 100.0]	[5.06, 8.97, 0.79]	$z<275$
Super-ellipsoid	[1.00, 1.00]	[185, 85, 295]	[55.0, 110.0, 64.0]	[0.00, 50.00, 0.00]	$x>150, z<280$
			Sternum		
Super-ellipsoid	[0.70, 0.50]	[151, 66, 176]	[17.5, 4.0, 12.0]	[28.00, 0.00, 0.00]	$z<185$
Torus	[18, 1.00]	[151, 105, 220]	[6.0, 3.0, 1.2]	[90.00, 67.00, 90.00]	$0.30y+0.96z<241.29$ $0.67y-0.74z<-91.56$
Super-ellipsoid	[0.80, 0.20]	[151, 44, 230]	[12.5, 3.0, 21.0]	[10.00, 0.00, 0.00]	$z>237$
Super-ellipsoid	[0.70, 0.50]	[151, 40, 255]	[6.0, 3.0, 12.0]	[9.00, 0.00, 0.00]	$z>247, z<267$
			Samples of vertebra		
Torus	[18, 1.00]	[150, −51, 240]	[10.0, 10.0, 8.0]	[0.00, 90.00, 0.00]	$-0.57y-0.82z<-167.34$ $-0.53y+0.85z<230.56$
Torus	[18, 1.36]	[150, −51, 240]	[10.0, 10.0, 8.0]	[0.00, 90.00, 0.00]	$-0.57y-0.82z<-167.37$ $0.53y+0.85z<176.51$
Torus	[18, 1.46]	[150, −51, 240]	[10.0, 10.0, 8.0]	[0.00, 90.00, 0.00]	$-0.52y-0.86z<-179.45$ $0.47y+0.88z<188.28$
Torus	[18, 2.00]	[150, −51, 240]	[10.0, 10.0, 8.0]	[0.00, 90.00, 0.00]	$0.36y-0.93z<-242.26$ $-0.43y+0.90z<238.58$
Torus	[18, 2.00]	[150, −51, 240]	[10.0, 10.0, 8.0]	[0.00, 90.00, 0.00]	$0.46y-0.88z<-236.43$ $-0.53y+0.85z<230.56$
			Samples of ribs		
Torus	[8, 0.67]	[164, 83, 154]	[2.0, 3.2, 3.2]	[−32.00, 0.00, 0.00]	$-0.99x-0.14y+0.09z-159.94$ $-0.74x-0.57y+0.35z<-115.06$
Torus	[8, 1.00]	[164, 83, 154]	[2.0, 3.2, 3.2]	[−32.00, 0.00, 0.00]	$-0.99x-0.14y+0.09z<-159.94$ $-0.74x-0.57y+0.35z<-115.06$
Torus	[8, 0.67]	[136, 83, 154]	[2.0, 3.2, 3.2]	[−32.00, 0.00, 0.00]	$-0.98x-0.15y+0.09z<135.80$ $0.80x-0.51y+0.32z<115.61$
Torus	[8, 1.00]	[136, 83, 154]	[2.0, 3.2, 3.2]	[−32.00, 0.00, 0.00]	$-0.98x-0.15y+0.09z<135.80$ $0.80x-0.51y+0.32z<115.61$
Torus	[12, 0.67]	[150, 91, 300]	[3.36, 5.12, 3.2]	[0.00, 32.00, 90.00]	$0.99x+0.11y-0.07z<137.91$ $-0.85y+0.53z<81.51$
Torus	[12, 1.00]	[150, 91, 300]	[3.36, 5.12, 3.2]	[0.00, 32.00, 90.00]	$0.99x+0.11y-0.07z<137.91$ $-0.85y+0.53z<81.51$
Torus	[12, 0.67]	[150, 91, 300]	[3.36, 5.12, 3.2]	[0.00, 32.00, 90.00]	$-0.85y+0.53z<81.51$ $-0.99x+0.11y-0.07z<-159.46$
Torus	[12, 1.00]	[150, 91, 300]	[3.36, 5.12, 3.2]	[0.00, 32.00, 90.00]	$-0.85y+0.53z<81.51$ $-0.99x+0.11y-0.07z<-159.46$
Torus	[12, 0.67]	[150, 83, 315]	[3.4, 5.08, 3.2]	[0.00, 32.00, 90.00]	$0.99x+0.11y-0.07z<136.22$ $-0.36x-0.79y+0.49z<35.98$
Torus	[12, 1.00]	[150, 83, 315]	[3.4, 5.08, 3.2]	[0.00, 32.00, 90.00]	$0.99x+0.11y-0.07z<136.22$ $-0.36x-0.79y+0.49z<35.98$
Torus	[12, 0.67]	[150, 83, 324]	[3.4, 5.04, 3.2]	[0.00, 32.00, 90.00]	$0.36x-0.79y+0.49z<144.11$ $-0.99x+0.11y-0.07z<-161.25$
Torus	[12, 1.00]	[150, 83, 324]	[3.4, 5.04, 3.2]	[0.00, 32.00, 90.00]	$0.36x-0.79y+0.49z<144.11$ $-0.99x+0.11y-0.07z<-161.25$

[a]For a superquadric, parameters $[e_1, e_2]$ refer to shape parameters e_1 and e_2, while for a torus the parameters $[R, r]$ refer to radius R and tube radius r.

[a]Electronic mail: jzhu@GeorgiaSouthern.edu
[b]Electronic mail: zhao@arch.cs.umsl.edu
[c]Electronic mail: yangbo-ye@uiowa.edu
[d]Electronic mail: ge-wang@uiowa.edu

[1]A. C. Kak and M. Slaney, *Principles of Computerized Tomographic Imaging* (Society for Industrial and Applied Mathematics, Philadelphia, 2001).
[2]I. G. Zubal, C. R. Harrell, E. O. Smith, Z. Rattner, G. Gindi, and P. B. Hoffer, "Computerized 3-dimensional segmented human anatomy," Med. Phys. **21**, 299–302 (1994).
[3]FORBILD Thorax phantom, http://www.imp.uni-erlangen.de/forbild/english/forbild/index.htm.
[4]W. P. Segars, D. S. Lalush, and B. M. W. Tsui, "A realistic spline-based dynamic heart phantom," IEEE Trans. Nucl. Sci. **46**, 503–506 (1999).
[5]W. P. Segars, "Development of a new dynamic NURBS-based cardiac-torso(NCAT) phantom," Ph.D. dissertation, The University of North Carolina, May 2001.
[6]W. P. Segars, D. S. Lalush, and B. M. W. Tsui, "Modeling respiratory mechanics in the MCAT and spline-based MCAT phantoms," IEEE Trans. Nucl. Sci. **48**, 89–97 (2001).
[7]A. Jaklic, A. Leonardis, and F. Solina, *Segmentation and Recovery of Superquadrics* (Kluwer Academic, New York, 2000).
[8]J. Peter, D. R. Gilland, R. J. Jaszczak, and R. E. Coleman, "Four-dimensional superquadric-based cardiac phantom for Monte Carlo simulation of radiological imaging system," IEEE Trans. Nucl. Sci. **46**, 2211–2217 (1999).
[9]J. Peter, M. P. Tornai, and R. J. Jaszczak, "Analytical versus voxelized phantom representation for Monte Carlo simulation in radiological imaging," IEEE Trans. Med. Imaging **19**, 556–564 (2000).
[10]A. S. Glassner, *An Introduction to Ray Tracing* (Academic, New York, 1989).
[11]A. H. Barr, "Superquadrics and angle preserving transformations," IEEE Comput. Graphics Appl. **1**, 11–23 (1981).
[12]A. H. Barr, "Global and local deformations of solid primitives," Comput. Graphics **18**, 21–30 (1984).
[13]R. Schmidt, "On the recognition of equations by Francois Vieta," in *The Early Theory of Equations. On their Nature and Constitutions* (Golden Hint Press, Annapolis, MD, 1986), pp. 1–104.
[14]L. A. Feldkamp, L. C. Davis, and J. W. Kress, "Practical cone-beam algorithm," J. Opt. Soc. Am. A **1**, 612–619 (1984).
[15]A. Kriete and L. C. Berger, Thorax Anatomy, http://www.med.uni-giessen.de/ipl/vae.html.
[16]J. Zhu, "Image reconstruction and geometric modeling in computed tomography," Ph.D. dissertation, The University of Iowa, July 2005.
[17]T. Nishita and T. W. Sederberg, "Ray tracing trimmed rational surface patches," Comput. Graphics **24**, 337–345 (1990).